Supplementary Information

Ultra-scaled Phototransistors based on Monolayer MoS_2

Thomas Schranghamer[1] and Saptarshi Das[1,2,3,4]

[1] *Engineering Science and Mechanics, Penn State University, University Park, PA 16802, USA*

[2] *Materials Science and Engineering, Penn State University, University Park, PA 16802, USA*

[3] *Materials Research Institute, Penn State University, University Park, PA 16802, USA*

[4] *Electrical Engineering and Computer Science, Penn State University, University Park, PA 16802, USA*

Supplementary Information 1

Material	Illumination Source	Response Time (s)	Active Area (um^2)	Active Volume (um^3)	Responsivity (A/W)	Detectivity (Jones)	Ref.
Conventional Ge	1550 nm	$6\cdot10^{-7}$	$7.1\cdot10^{6}$	N/A	0.85	N/A	2
Conventional InGaAs	1200 nm	$3\cdot10^{-10}$	10^{4}	N/A	1.003	N/A	3
Conventional Si	850 nm	$0.35/2\cdot10^{-10}$	$1.8\cdot10^{4}$	N/A	~0.36	N/A	3
1L BiOBr	Laser, 245 nm	$1.02\cdot10^{-4}$	~5.19	~0.0030	$1.27\cdot10^{4}$	$8.37\cdot10^{12}$	4
1L Graphene on Si	Laser, 155 nm	N/A	~1.55	$\sim5.35\cdot10^{-4}$	0.37	N/A	5
1L Graphene on Si	Laser, 850 nm	N/A	~128	~0.0442	70	$2\cdot10^{13}$	6
1L MoS_2	Laser, 561 nm	4/9	~ 2.5	~0.00163	880	$2\cdot10^{9}$	7
1L MoS_2	Laser, 450-800 nm	$5/5\cdot10^{-2}$	5.46	0.00393	0.0075	N/A	8
1L MoS_2 (CVD)	Laser, 405 nm	0.9/2.2	65	0.04225	$1.55\cdot10^{-4}$	$4.07\cdot10^{14}$	9
1L MoS_2 (CVD)	Laser, 520 nm	4.1/0.2	15.96	0.0104	$3.4\cdot10^{7}$	$4.3\cdot10^{16}$	10
1L $MoSe_2$	Laser, 650 nm	$2.5\cdot10^{-2}$	$9\cdot10^{4}$	~63	N/A	N/A	11
1L $PtSe_2$	Laser, 633 nm	$1.2\cdot10^{-3}$	15.4 - 18.1	0.0097 - 0.0114	0.9	N/A	12
1L SnS	Laser, 660 nm	$1.2\cdot10^{-4}$	50	0.035	920	$1.09\cdot10^{9}$	13
3L BiOBr	Laser, 245 nm	$1.02\cdot10^{-4}$	~5.19	0.0187	$1.27\cdot10^{4}$	$8.37\cdot10^{12}$	4
3L MoS_2	Laser, 532 nm	$0.7/1.1\cdot10^{-4}$	$7.9\cdot10^{4}$	154	0.57	10^{10}	14
Bi_2S_3 nanobelt	Lamp, 800 nm	$0.5/2\cdot10^{-4}$	~150	~15	201	$2.7\cdot10^{10}$	15
Bi_2Se_3 on Si	Laser, 808 nm	$2.5/5.5\cdot10^{-6}$	$3\cdot10^{6}$	$> 3\cdot10^{4}$	24.3	$4.39\cdot10^{12}$	16
CdS nanowires on Si pyramids	Laser, 1064 nm	N/A	$2.25\cdot10^{6}$	$> 1.5\cdot10^{6}$	14.2	$1.65\cdot10^{12}$	17
CdS on Si	Laser, 442 nm	$3.68/4.4\cdot10^{-4}$	$1.6\cdot10^{7}$	> 1018	0.0041	$9.2\cdot10^{11}$	18
$CH_3NH_3PbI_3$	Laser, 265 nm	$2.2/4\cdot10^{-3}$	100	6	12	$\sim10^{11}$	19
Cs-doped $FAPbI_3$ on SI nanorods	Laser, 850 nm	$4/8\cdot10^{-6}$	$2.5\cdot10^{7}$	$3.75\cdot10^{8}$	0.844	$3.2\cdot10^{11}$	20
$CuInSe_2$ nanosheet	N/A, 254 - 700 nm	10.5/8.4	200	> 1.5	1900	$7\cdot10^{11}$	21
CuO on Si nanowires on In:Ga	Laser, 532 nm	$6/8\cdot10^{-5}$	$2\cdot10^{6}$	$> 10^{7}$	1.05·10·	10^{9}	22
Few-layer AsP/InSe	Laser, 520 nm	$2.17\cdot10^{-4}$	> 26.1	> ~0.56	1	10^{12}	23
Few-layer Bi_2O_2Se	Laser, 405 nm	$3.2/9.8\cdot10^{-5}$	159.12	2.23	$5.01\cdot10^{4}$	$8.2\cdot10^{12}$	24
Few-layer BP	Laser, 532 nm	N/A	~100	> 0.7	1.16	N/A	25
Few-layer BP	Laser, 640 nm	10^{-3}	~80	~0.64	0.0048	N/A	26
Few-layer BP	Laser, 3680 nm	N/A	~500	~11.5	23	N/A	27
Few-layer BP	Laser, 580 nm	N/A	~320	~9.6	~6	N/A	28
Few-layer BP	Laser, 633 nm	$5\cdot10^{-3}$	0.45	0.0036	$4.3\cdot10^{6}$	N/A	29

Few-layer BP	Laser, 520 nm	N/A	~28	~0.28	2	N/A	30
Few-layer BP-carbide	Laser, 2000 nm	$7\cdot10^{-10}$	~50	~0.375	2163	$\sim10^{11}$	31
Few-layer $CuGaSe_2$	Lamp, 254 - 700 nm	1.6/6.6	350	> 2.1	103	$8\cdot10^{11}$	32
Few-layer GaS	Laser, 254 nm	$3\cdot10^{-2}$	200	0.45	4.2	N/A	33
Few-layer GaSe	Laser, 254-700 nm	$2\cdot10^{-2}$	> ~600	> 2.4	2.8	N/A	34
Few-layer GaTe	Laser, 532 nm	6	~50	~0.5	10^{4}	N/A	35
Few-layer graphene with Au antennas	Laser, 4000 nm	10^{-4}	40	0.0276	$1.66\cdot10^{-5}$	$5\cdot10^{6}$	36
Few-layer In_2Se_3	Laser, 300 nm	$1.8\cdot10^{-2}$	0.108	0.00108	395	$2.26\cdot10^{12}$	37
Few-layer In_2Se_3	Laser, 405 - 940 nm	9	~2	~0.028	$9.8\cdot10^{4}$	$\sim3.3\cdot10^{13}$	38
Few-layer InSe	Laser, 543 nm	$6\cdot10^{-5}$	10	> 0.0083	4.86	N/A	39
Few-layer InSe and Au NPs	Laser, 685 nm	$2.5/2.5\cdot10^{-2}$	60	1.8	0.244	$\sim5\cdot10^{12}$	40
Few-layer InSe doped with $AuCl_3$	LED, 470 nm	N/A	71	0.994	$1.93\cdot10^{4}$	$3\cdot10^{13}$	41
Few-layer InSe/BP	Laser, 4000 nm	$1.5/4\cdot10^{-4}$	4	0.08	80	N/A	42
Few-layer MoS_2	Laser, 532 nm	$2\cdot10^{-5}$	22.5 - 62.4	0.099 - 0.150	12	$> 10^{13}$	43
Few-layer MoS_2	Laser, 637 nm	$4.8\cdot10^{-4}$	20 - 100	> 0.029 - 0.14	3260	$9\cdot10^{14}$	44
Few-layer MoS_2 on Si	Laser, 580 nm	$1/1.9\cdot10^{-5}$	100	1	8.73	$1.12\cdot10^{12}$	45
Few-layer MoS_2/BP	Laser, 3800 nm	$3\cdot10^{-6}$	> 382	> 61	0.9	$1.1\cdot10^{10}$	46
Few-layer $MoSe_2$	Laser, 532 nm	$1.5\cdot10^{-2}$	~580	~11.6	97.1	N/A	47
Few-layer $MoTe_2$	Laser, 532 nm	$3\cdot10^{-5}$	~230	~2.75	5	$3\cdot10^{12}$	48
Few-layer $MoTe_2$	Laser, 1265 nm	$< 10^{-9}$	~3 - 6	~0.033 - 0.27	0.15	N/A	49
Few-layer $MoTe_2$	Laser, 1550 nm	N/A	~270	~10.80	0.01	N/A	50
Few-layer $MoTe_2$ on Si	Laser, 980 nm	$1.5\cdot10^{-7}$	$5.6\cdot10^{7}$	$2.32\cdot10^{5}$	0.19	$6.8\cdot10^{13}$	51
Few-layer $MoTe_2$/Graphene/SnS_2	Laser, 1064 nm	$2.86\cdot10^{-2}$	23.3	~0.284	2600	$1.1\cdot10^{13}$	52
Few-layer $Pb_{1-x}Sn_xSe$	Laser, 375 - 980 nm	0.9/0.74	32.93	> 0.494	5.95	N/A	53
Few-layer $PdSe_2$	Laser, 780 nm	N/A	10^{7}	$> 1.2\cdot10^{4}$	0.3	$1.18\cdot10^{13}$	54
Few-layer ReS_2	Laser, 532 nm	> 10	2.28	0.00912	$8.86\cdot10^{4}$	$1.18\cdot10^{12}$	55
Few-layer SnS_2	Laser, 350 nm	$2/1.6\cdot10^{-2}$	~9.41	0.0941	261	10^{10}	56
Few-layer $SnSe_2$	LDLS, 530 nm	$1.45/0.8\cdot10^{-2}$	~11.35	~0.0170	1100	10^{10}	57
Few-layer $Sr_2Nb_3O_{10}$	Lamp, 270 nm	$0.04/4\cdot10^{-2}$	~3.63	~0.0446	1214	$1.4\cdot10^{14}$	58
Few-layer Te	Laser, 1700 nm	N/A	10.2	0.102 - 0.204	16	$2\cdot10^{9}$	59
Few-layer WS_2	Laser, 458-647 nm	$5.3\cdot10^{-3}$	$> 2.5\cdot10^{4}$	> 200	$9.2\cdot10^{-5}$	N/A	60
Few-layer WS_2	Laser, 532 nm	N/A	~5	~0.005	2.5	$9.9\cdot10^{10}$	61
Few-layer WS_2/HfS_2	Laser, 4700 nm	$2.2\cdot10^{-3}$	6	0.0162	1535	N/A	62
Few-layer WSe_2	Laser, 852 nm	$5.37\cdot10^{-2}$	128	~0.23 - 1.28	2	$7.2\cdot10^{10}$	63

Few-layer WSe_2 (CTAB-doped)	Laser, 450 nm	$7.8\cdot10^{-3}$	~2.75	~0.0055	30	$1.25\cdot10^{11}$	64
Ge	Laser, 1550 nm	N/A	153.9	53.865	0.62	N/A	65
Ge	Laser, 1310-1480 nm	N/A	0.009	$7.2\cdot10^{-4}$	N/A	N/A	66
Ge	Laser, 1300 nm	N/A	15	2.1	0.4	N/A	67
Ge	Laser, 532 nm	$7/0.6\cdot10^{-2}$	~10	> 0.085	200	$1.06\cdot10^{10}$	68
Ge (nanowire)	Laser, 532 nm	N/A	0.0125	$9.82\cdot10^{-4}$	$8.9\cdot10^{4}$	10^{11}	69
Ge (nanowire)	Laser, 532 nm	N/A	$5.4\cdot10^{-4}$	$1.27\cdot10^{-5}$	~8000	N/A	70
Ge (photocavity-enhanced)	Laser, 733 nm	N/A	1250	21.5	4.7	N/A	71
GeSn/Ge dual-nanowire	Laser, 2000 nm	N/A	~0.45 - 1.00	~0.053 - 0.157	$1.2\cdot10^{-6}$	N/A	72
Graphene and Ti_2O_3 NPs	Laser, 10000 nm	$2.6\cdot10^{-3}$	210.6	> ~0.218	300	$7\cdot10^{8}$	73
Graphene on Si	Laser, 890 nm	$3.2/7.5\cdot10^{-4}$	10^{7}	> $7.8\cdot10^{4}$	0.73	$5.77\cdot10^{13}$	74
Graphene/Ta_2O_5/Graphene	Laser, 532 nm	N/A	12.9 - 24	0.073 - 0.137	~1000	N/A	75
InAs nanorods on Si (vertical)	Laser, 300 - 3000 nm	N/A	$2.56\cdot10^{5}$	$1.54\cdot10^{5}$	0.16	N/A	76
InGaAs nanowire	Laser, 1346 nm	N/A	~0.0198	~0.001188	0.68	N/A	77
InGaAs on Si	Laser, 400−1250 nm	$1.3\cdot10^{-2}$	2500	500	7520	N/A	78
Many-layer WSe_2/ZnO	Laser, 405 nm	$1.65\cdot10^{-4}$	~95.73	> 7.85	4830	$1.56\cdot10^{13}$	79
NiO NPs on ZnO nanowire	Halogen lamp, 365 nm	133.5	0.688	0.0865	N/A	N/A	80
PbS QDs with Ag nanoparticles	Lamp, 400 - 1200 nm	$\sim10^{-3}$	$5\cdot10^{6}$	$\sim3\cdot10^{4}$	>20	$6\cdot10^{12}$	81
PbSe QDs (~2500 arranged in line)	Laser, 532 nm	$2/3\cdot10^{-7}$	0.04	$\sim8.38\cdot10^{-5}$	3.9	N/A	82
Perovskite nanowires	LED, 530 nm	$2.8/2.5\cdot10^{-5}$	~25	~7.85	$1.5\cdot10^{4}$	$7\cdot10^{15}$	83
Perovskite on TiO_2 on Si	Laser, 800 nm	$1.16/5\cdot10^{-2}$	$2.4\cdot10^{7}$	$8.4\cdot10^{7}$	0.87	$6\cdot10^{12}$	84
Se nanorods on Si	Laser, 610 nm	$0.2/1.7\cdot10^{-3}$	$4.19\cdot10^{4}$	N/A	0.374	$4.39\cdot10^{11}$	85
Si	N/A, 400 nm	< $2\cdot10^{-2}$	0.1118	0.00559	N/A	$4.3\cdot10^{12}$	86
Si nanowire with Au shell	Lamp, white light	N/A	0.15	0.00589	N/A	N/A	87
SnS nanobelt	Laser, 800 nm	$4.3\cdot10^{-2}$	~4.5	0.144	300	$6\cdot10^{9}$	88
SnTe	Laser, 254 - 4650 nm	$2.1/7.3\cdot10^{-7}$	~0.007	$\sim8.4\cdot10^{-4}$	71.11	N/A	89
TiO_2 nanorods on Si	Laser, 600 nm	N/A	$1.9\cdot10^{7}$	$3.2\cdot10^{7}$	10^{-6}	N/A	90
Vertical MoS_2 on Si	Laser, 808 nm	$0.3/4\cdot10^{-5}$	$9\cdot10^{6}$	$1.35\cdot10^{7}$	0.3	10^{13}	91
Vertical $MoSe_2$ on Si	Laser, 650 nm	$2.7/3.5\cdot10^{-4}$	$7.07\cdot10^{6}$	$1.4\cdot10^{7}$	0.27	$7.13\cdot10^{10}$	92
ZnO nanowires on Si	Laser, 442 nm	0.101	$6.4*10^{5}$	> $6.4\cdot10^{7}$	7100	$7.1\cdot10^{9}$	93
α-In_2Te_3	Laser, 370 - 1064 nm	$1.5\cdot10^{-2}$	$3\cdot10^{4}$	660	44	$6\cdot10^{12}$	94
γ-In_2Se_3 on Si	Laser, 820 nm	$1.8/2.3\cdot10^{-4}$	$2.5\cdot10^{5}$	5000	5.67	$5.66\cdot10^{13}$	95
1L MoS_2 (MOCVD)	LED, 450 nm	$1/1\cdot10^{-3}$	0.0065	$4.23\cdot10^{-6}$	$8.84\cdot10^{8}$	$7.13\cdot10^{12}$	This Work

Table S1. Benchmarking table of low-dimensional photodetectors. *Comparison between this work and other notable works concerning the fabrication and characterization of photodetectors based on low-dimensional materials. Based on this literature survey, the active volume of the ultra-scaled monolayer-MoS_2-based phototransistor reported in this work is ~3× smaller than the previously-reported smallest photodetector. Note that we are also aware of the work by Lin et al.*[1] *in which they report a photodetector based on single-crystal $CH_3NH_3PbI_3$ with an active area of ~20 nm^2. We have chosen to omit that work from this table due to the unscalable nature of the fabrication process used, as it relies upon the random development of nanogaps in carbon nanotubes during drop-casting.*

Supplementary Information 2

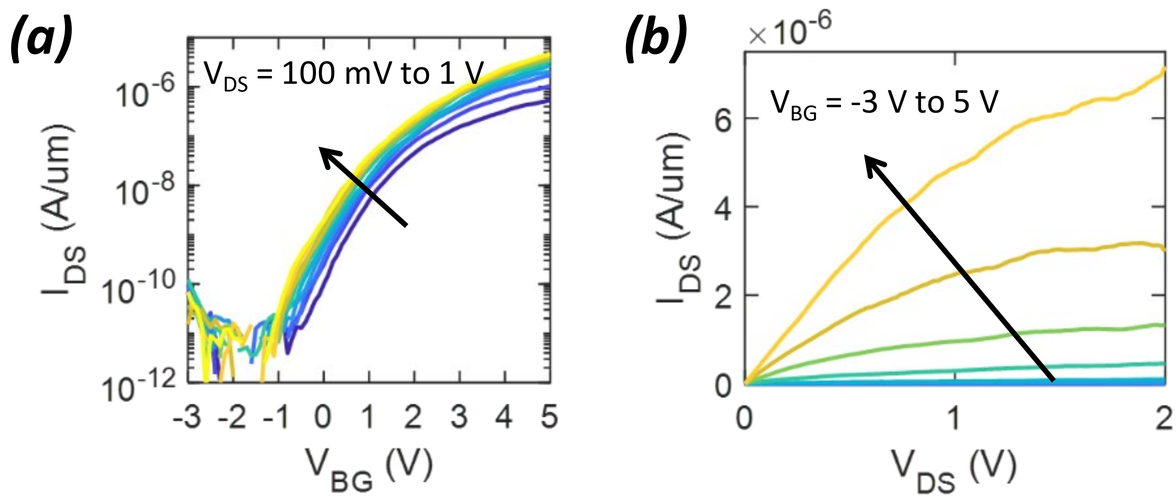

Figure S1. Electrical characterization of a representative MoS_2 phototransistor. a) *Transfer characteristics, i.e., source-to-drain current (I_{DS}) as a function of the local back-gate voltage (V_{BG}), when source-to-drain voltage (V_{DS}) is varied from 100 mV to 1 V in steps of 100 mV. The change in threshold voltage (V_{th}) with V_{DS} is indicative of drain-induced barrier lowering as a result of small L_{ch}.* ***b)*** *The output characteristics, i.e., I_{DS} versus V_{DS}, at varying V_{BG} for the same device as in (a).*

Supplementary Information 3

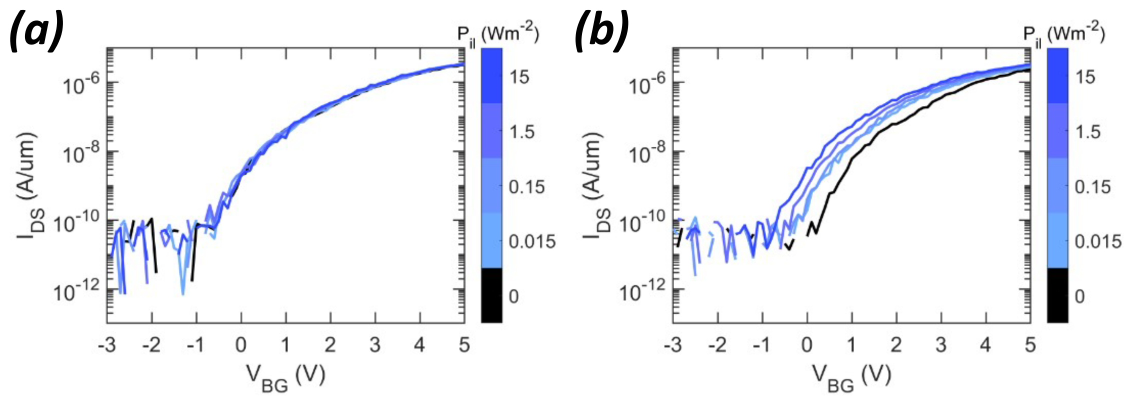

Figure S2. Photogating in ultra-scaled MoS_2 ***phototransistors. a-b)*** *Post-illumination transfer characteristics of a representative phototransistor measured at* $V_{DS} = 1$ *V in dark after* $\tau_{exp} = 1$ *s exposure to* P_{il} *spanning four orders of magnitude (0.015* Wm^{-2} *to 15* Wm^{-2}*) for blue light (*λ *= 450 – 455 nm). During illumination the device was biased both in the ON-state (a) and in the OFF-state (b) by applying a voltage (*V_{exp}*) of 2 V and -2 V, respectively, to the global back-gate. Significant and persistent changes in the transfer characteristics were only seen when the device was biased in the OFF-state, indicating the presence of the photogating effect.*

Supplementary Information 4

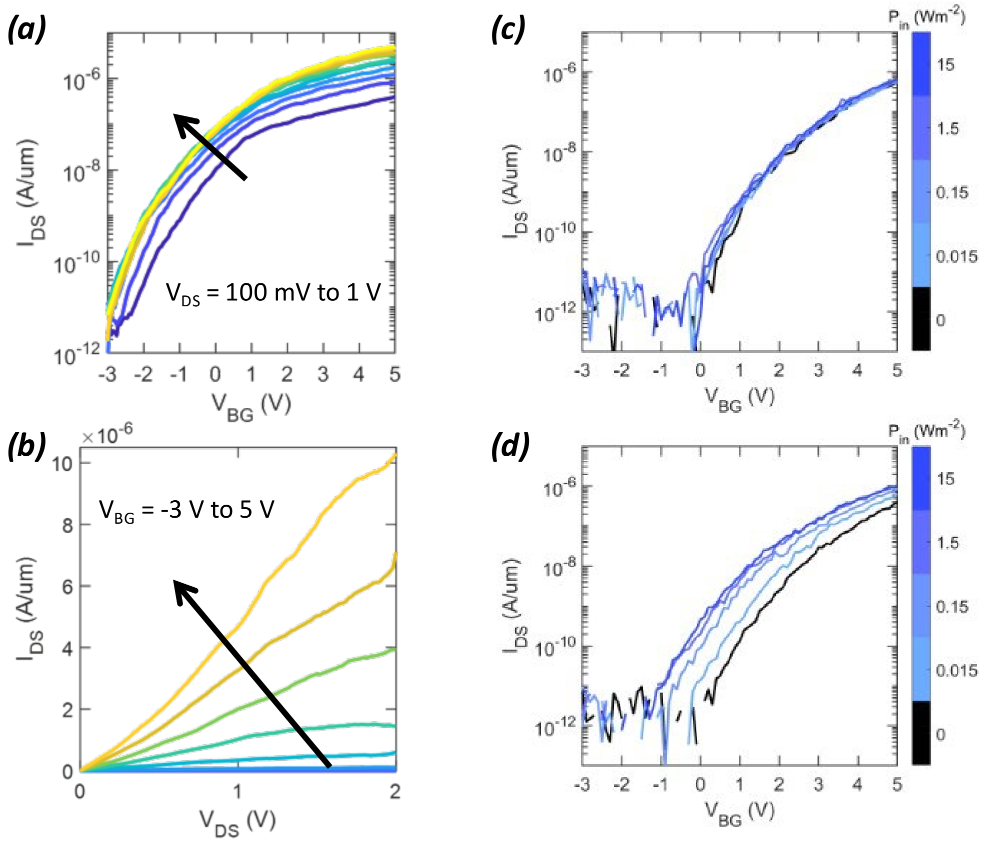

Figure S3. Contact scaling of MoS_2 phototransistors. a) *Transfer characteristics, i.e., source-to-drain current (I_{DS}) as a function of the local back-gate voltage (V_{BG}), when source-to-drain voltage (V_{DS}) is varied from 100 mV to 1 V in steps of 100 mV for an MoS_2 phototransistor with a channel length (L_{ch}) of 20 nm, a channel width of 400 nm, and a contact length (L_c) of 40 nm. The change in threshold voltage (V_{th}) with V_{DS} is indicative of drain-induced barrier lowering as a result of small L_{ch}.* ***b)*** *The output characteristics, i.e., I_{DS} versus V_{DS}, at varying V_{BG} for the same device as in (a). The device shows more Schottky-like behavior than the device in Fig. 1, which may be a result increased current crowding due to L_c-scaling.* ***c-d)*** *Post-illumination transfer characteristics of the same device as in (a-b) measured at V_{DS} = 1 V in dark after τ_{exp} = 1 s exposure to P_{il} spanning four orders of magnitude (0.015 Wm^{-2} to 15 Wm^{-2}) for blue light (λ = 450 – 455 nm). During illumination the device was biased both in the ON-state (c) and in the OFF-state (d) by applying a voltage (V_{exp}) of 2 V and -2 V, respectively, to the global back-gate. Significant and persistent changes in the transfer characteristics were only seen when the device was biased in the OFF-state, indicating the presence of the photogating effect. The presence of the photogating effect in an MoS_2 phototransistor with scaled contacts (L_c = 40 nm) indicates that the total device area can be reduced by almost half (to 0.040 μm^2) without overtly sacrificing its photodetecting capabilities.*

Supplementary Information 5

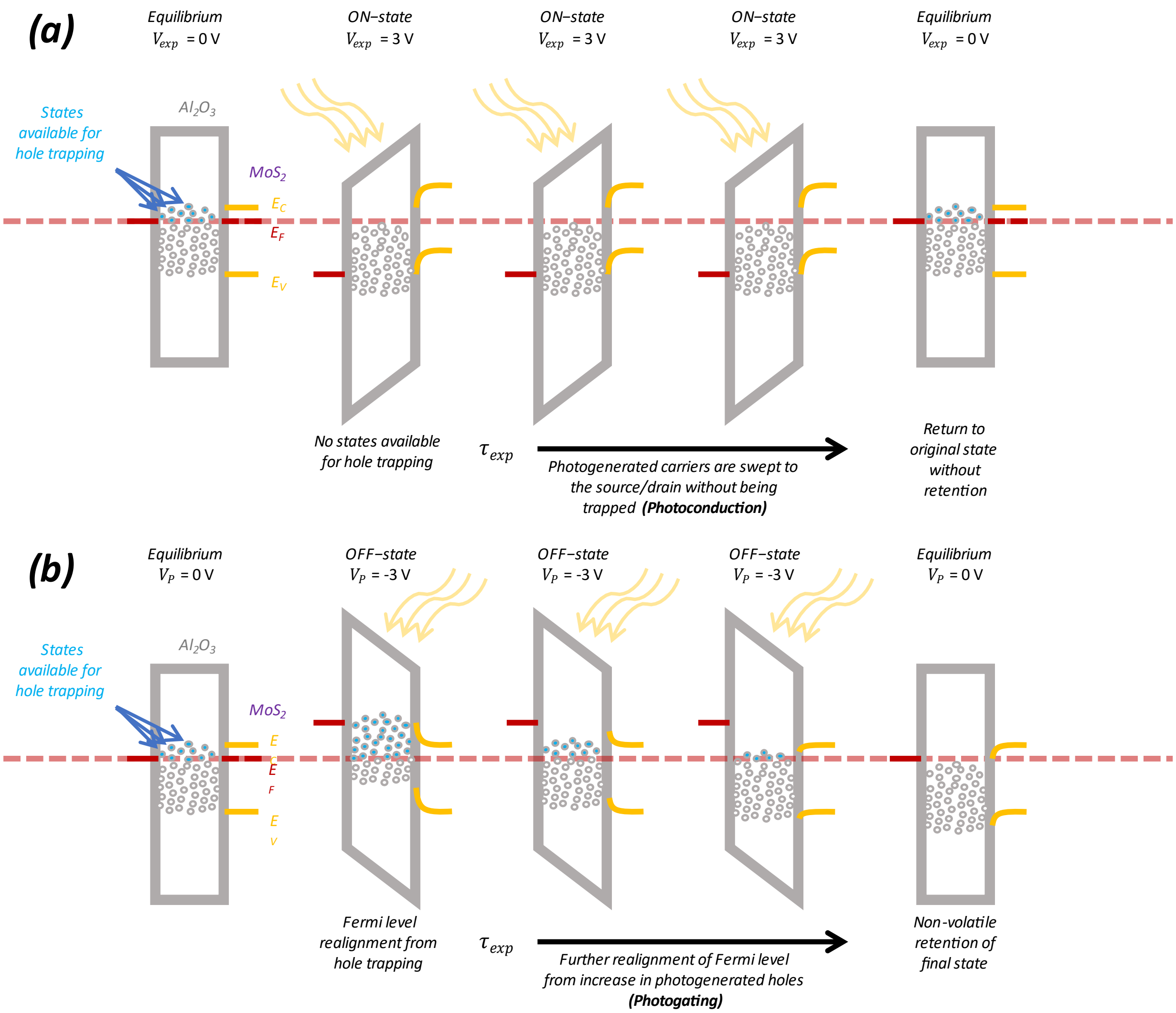

Figure S4. Photoconduction and photogating in MoS_2 phototransistors. *Band diagrams explaining the origins explaining the origins of the photoconduction effect and the photogating effect when the device is biased (V_{exp}) in the* ***a)*** *ON-state and* ***b)*** *OFF-state during illumination, respectively. In the ON-state, i.e., when V_{exp} is positive, When the device is in equilibrium, all trap states (interface traps, deep oxide traps, etc.) below the Fermi energy (E_F) are filled, while all trap states above the Fermi energy (E_F) remain empty. When the device is biased in the ON-state, i.e., when a positive V_{exp} is applied to the gate, most trap states lie below E_F; this makes trapping of photogenerated holes under illumination unlikely, thus preventing any display of photogating and persistent photoconductance. However, when the device is biased in the OFF-state, i.e., when a negative V_{exp} is applied, most trap states will be brought above E_F, making hole trapping significantly more probable. These trapped holes then realign the Fermi level, shifting the threshold voltage (V_{th}) of the device. The more photogenerated holes available, i.e., the higher P_{il} and the longer τ_{exp}, the more of these trap states that will be filled and the greater the shift in V_{th}.*

Supplementary Information 6

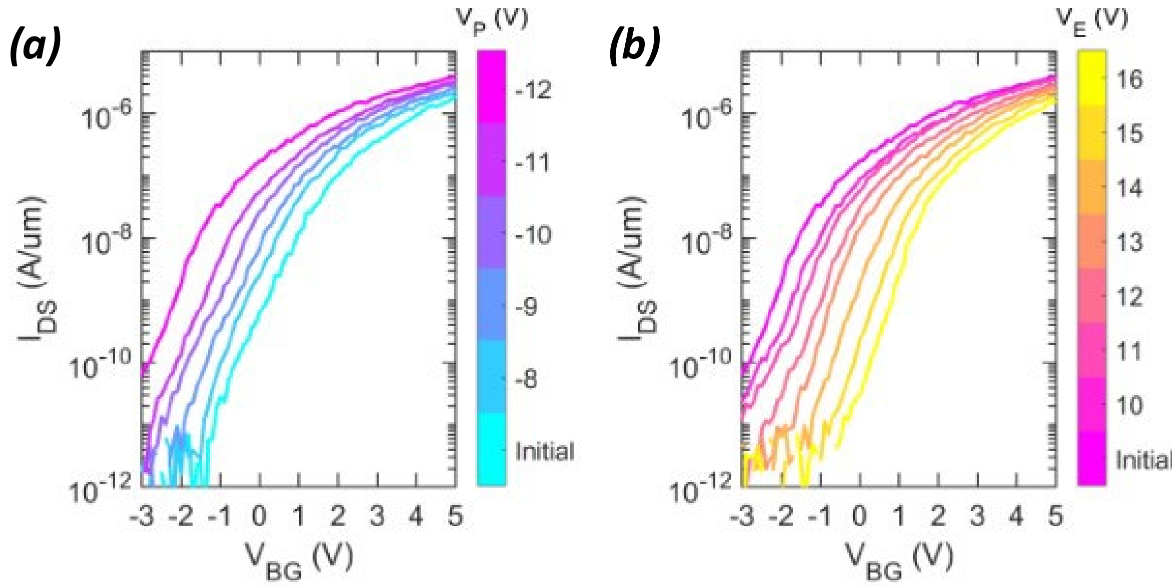

Figure S5. Non-volatile program/erase operations in MoS_2 phototransistors. a) *Transfer characteristics of an MoS_2 phototransistor when negative programming voltage pulses (VP) of duration (τ_{pulse}) 1 ms with increasing magnitude are applied to the back-gate, starting at -8 V and increasing to -12 V in steps of -1 V. The source and drain terminals are kept grounded during this process. A negative shift in the threshold voltage (V_{th}) can be clearly seen, indicating electrostatically-induced hole trapping similar to that observed in the photogating effect. The magnitude of the shift monotonically increases with increasing V_P and τ_{pulse} just as the shift induced by photogating increases with V_{exp} and τ_{exp}.* ***b)*** *Transfer characteristics of the same MoS_2 phototransistor as in (a) when negative programming voltage pulses (V_E) with τ_{pulse} = 1 ms and increasing magnitude are applied to the back-gate, starting at 10 V and increasing to 16 V in steps of 1 V. A positive shift in Vth can be clearly seen, indicating hole de-trapping and/or electron trapping, with the magnitude of the shift varying based on the magnitude of V_E and τ_{pulse}. Additionally, increasing the magnitude of V_E is shown to increase the post-illumination to post-reset current ratio (CR), indicating that the resetting process can be tailored for different P_{il}.*

Supplementary Information 7

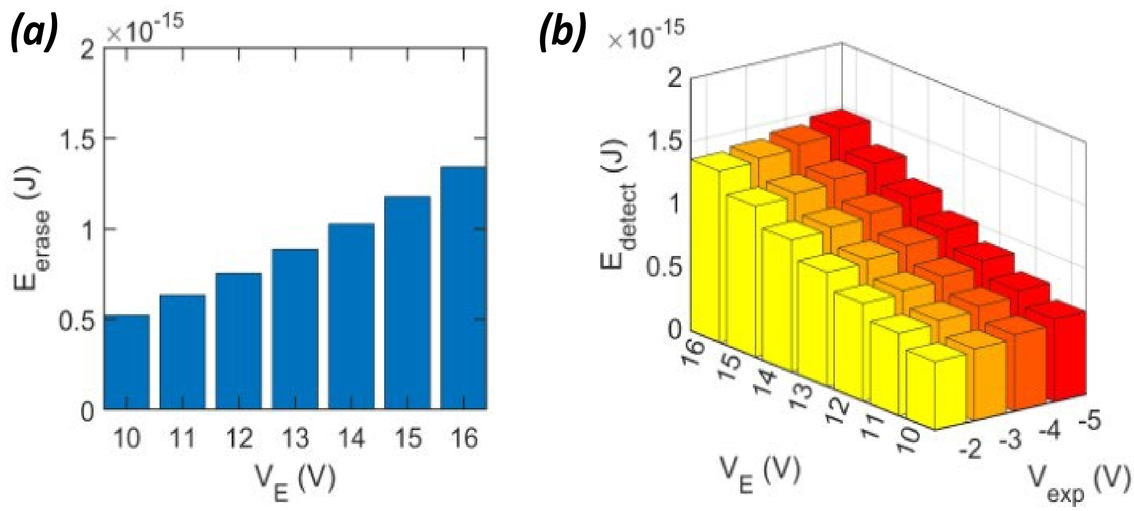

Figure S6. Energy expenditure of light detection. a) *Bar plot of the energy expenditure for each erase operation (E_{erase}) as a function of V_E, as given by the approximation* $E_{erase} \approx \frac{1}{2}C_G {V_E}^2$*.* ***b)*** *Bar plot of the total energy expenditure a detection operation (E_{detect}) as a function of V_E and V_{exp}. This relationship is given by the approximation* $E_{detect} = E_{exp} + E_{erase} \approx \frac{1}{2}C_G {V_{exp}}^2 + \frac{1}{2}C_G {V_E}^2$*.*

Supplementary Information 8

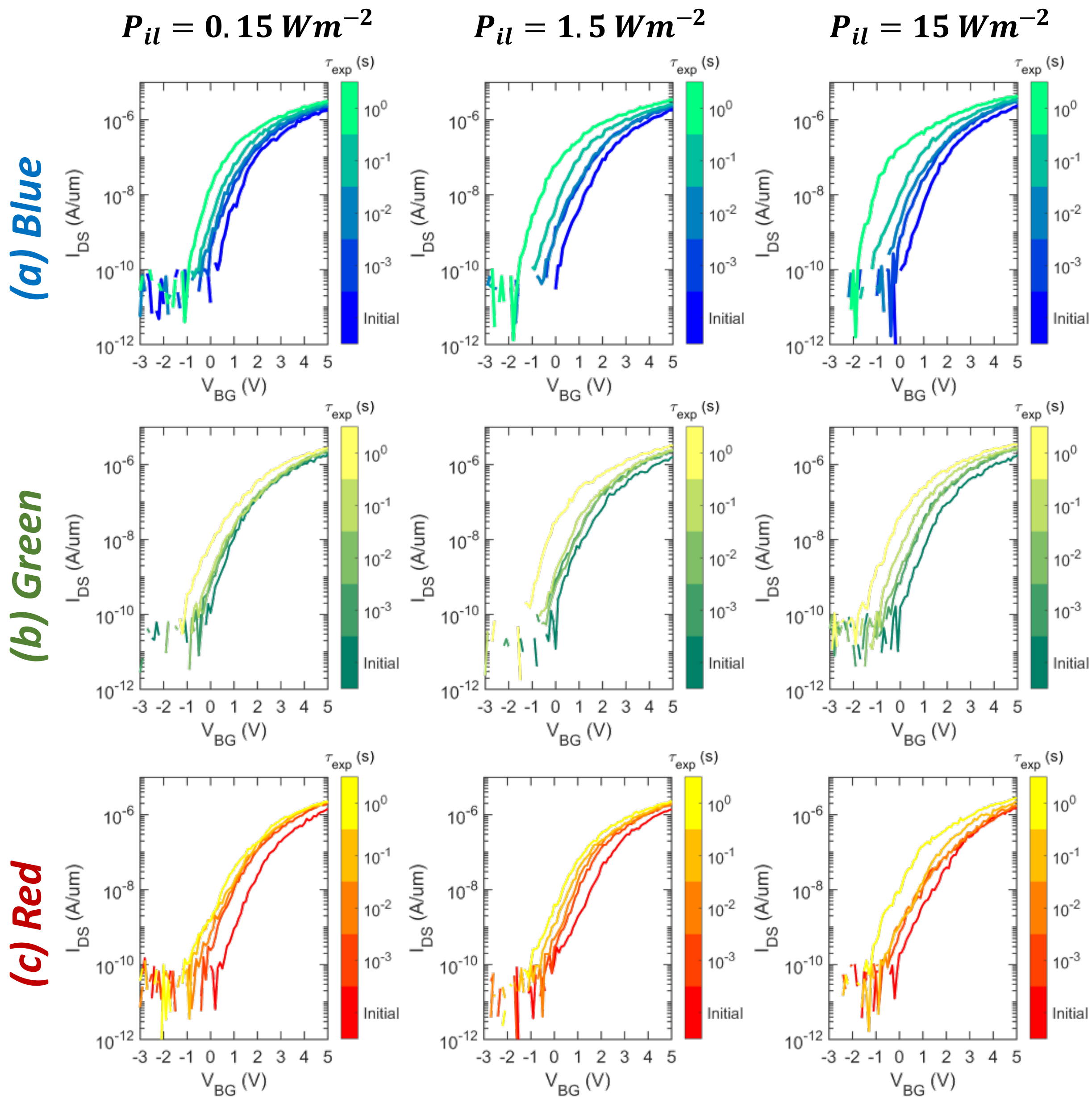

***Figure S7. Transfer characteristics for photocurrent extraction at V_{exp} = -3 V.** Transfer characteristics following illumination under **a)** blue, **b)** green, and **c)** red wavelengths at V_{exp} = - 3 V and varying τ_{exp} and P_{il} used for extraction of the photocurrent shown in **Figure 2a-c**.*

Supplementary Information 9

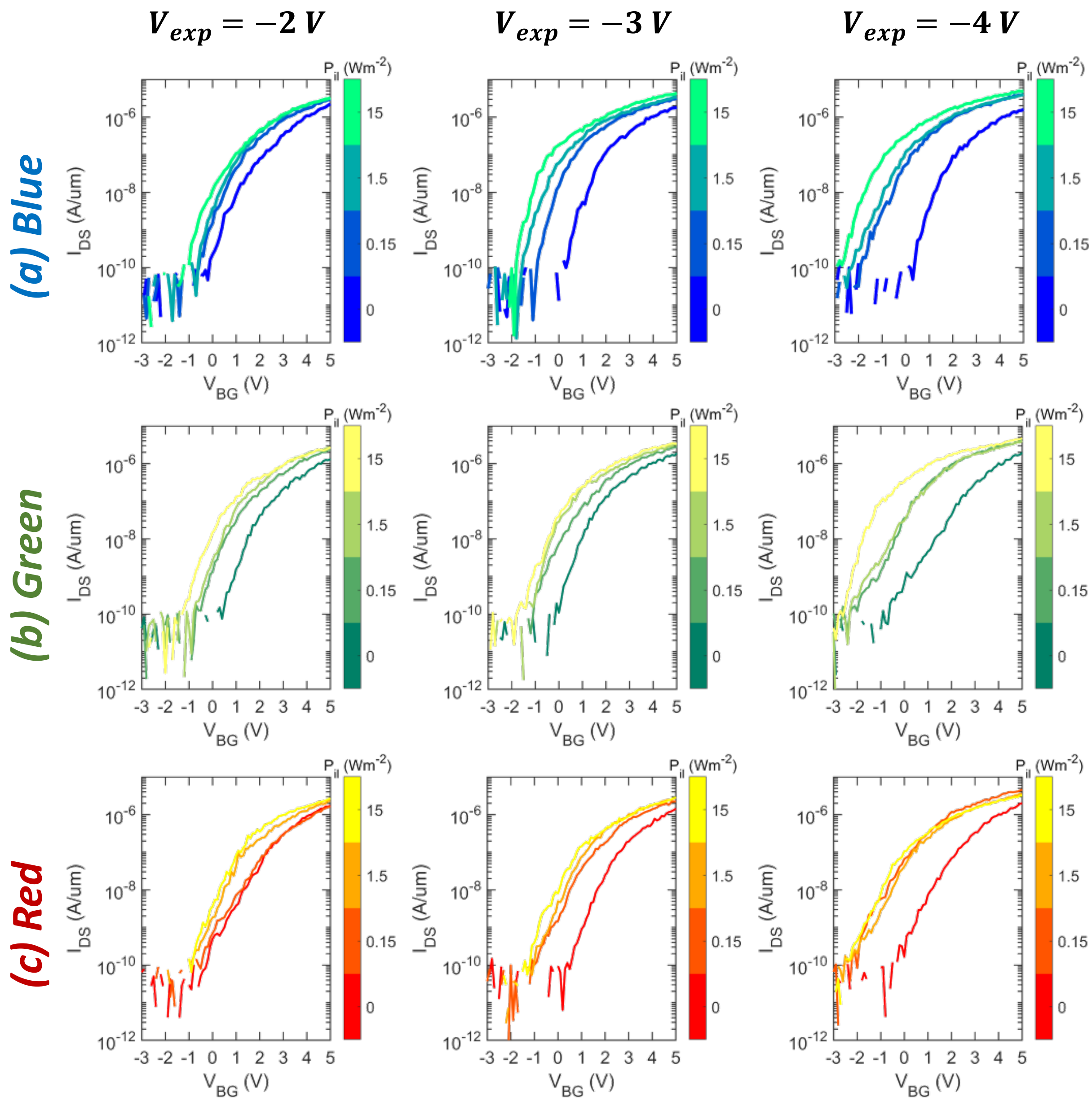

Figure S8. Transfer characteristics for photocurrent extraction at τ_{exp} = 1 s. *Transfer characteristics following illumination under a) blue, b) green, and c) red wavelengths at τ_{exp} = 1 s and varying V_{exp} and P_{il} used for extraction of the photocurrent shown in **Figure 2d-f**. Note that the MoS_2 phototransistor used for these measurements was reset between each experiment using the mechanisms discussed in **Fig. S4-S5**.*

References

1 Lin, Y., Lin, G., Sun, B. & Guo, X. Nanocrystalline Perovskite Hybrid Photodetectors with High Performance in Almost Every Figure of Merit. *Advanced Functional Materials* **28** (2018).

2 Radisavljevic, B. & Kis, A. Mobility engineering and a metal-insulator transition in monolayer MoS(2). *Nat Mater* **12**, 815-820, doi:10.1038/nmat3687 (2013).

3 Cui, X. *et al.* Multi-terminal transport measurements of MoS2 using a van der Waals heterostructure device platform. *Nat Nanotechnol* **10**, 534-540, doi:10.1038/nnano.2015.70 (2015).

4 Gong, C. *et al.* Large-Scale Ultrathin 2D Wide-Bandgap BiOBr Nanoflakes for Gate-Controlled Deep-Ultraviolet Phototransistors. *Advanced Materials* **32** (2020).

5 Goykhman, I. *et al.* On-Chip Integrated, Silicon–Graphene Plasmonic Schottky Photodetector with High Responsivity and Avalanche Photogain. *Nano Letters* **16**, 3005-3013 (2016).

6 Chang, K. E. *et al.* Gate-Controlled Graphene–Silicon Schottky Junction Photodetector. *Small* **14** (2018).

7 Lopez-Sanchez, O., Lembke, D., Kayci, M., Radenovic, A. & Kis, A. Ultrasensitive photodetectors based on monolayer MoS_2. *Nature Nanotechnology* **8**, 497-501 (2013).

8 Yin, Z. *et al.* Single-Layer MoS_2 Phototransistors. *ACS Nano* **6**, 74-80 (2012).

9 Jian, J., Chang, H., Dongc, P., Baic, Z. & Zuoc, K. A mechanism for the variation in the photoelectric performance of a photodetector based on CVD-grown 2D MoS_2. *RSC Advances* **11**, 5204-5217 (2021).

10 Seo, J. *et al.* Ultrasensitive Photodetection in MoS_2 Avalanche Phototransistors. *Advanced Science* **8** (2021).

11 Chang, Y.-H. *et al.* Monolayer $MoSe_2$ Grown by Chemical Vapor Deposition for Fast Photodetection. *ACS Nano* **8**, 8582-8590 (2014).

12 Yu, X. *et al.* Atomically thin noble metal dichalcogenide: a broadband mid-infrared semiconductor. *Nature Communications* **9**, 1-9 (2018).

13 Krishnamurthi, V. *et al.* Liquid-Metal Synthesized Ultrathin SnS Layers for High-Performance Broadband Photodetectors. *Advanced Materials* **32** (2020).

14 Tsai, D.-S. *et al.* Few-Layer MoS_2 with High Broadband Photogain and Fast Optical Switching for Use in Harsh Environments. *ACS Nano* **7**, 3905-3911 (2013).

15 Xu, J. *et al.* Synthesis of bismuth sulfide nanobelts for high performance broadband photodetectors. *Journal of Materials Chemistry C* **8**, 2102-2108 (2020).

16 Zhang, H., Zhang, X., Liu, C., Lee, S.-T. & Jie, J. High-Responsivity, High-Detectivity, Ultrafast Topological Insulator Bi_2Se_3/Silicon Heterostructure Broadband Photodetectors. *ACS Nano* **10**, 5113-5122 (2016).

17 Dai, Y. *et al.* Enhanced performances of Si/CdS heterojunction near-infrared photodetector by the piezo-phototronic effect. *Nano Energy* **44**, 311-318 (2018).

18 Dai, Y. *et al.* Self-Powered Si/CdS Flexible Photodetector with Broadband Response from 325 to 1550 nm Based on Pyro-phototronic Effect: An Approach for Photosensing below Bandgap Energy. *Advanced Materials* **30** (2018).

19 Zheng, W. *et al.* An ultrafast-temporally-responsive flexible photodetector with high sensitivity based on high-crystallinity organic–inorganic perovskite nanoflake. *Nanoscale* **9**, 12718-12726 (2017).
20 Liu, J.-Q. *et al.* Silicon/Perovskite Core–Shell Heterojunctions with Light-Trapping Effect for Sensitive Self-Driven Near-Infrared Photodetectors. *ACS Applied Materials & Interfaces* **10**, 27850–27857 (2018).
21 Liu, H., Yu, M., Qin, F., Feng, W. & Hu, P. Two-Dimensional Nonlayered $CuInSe_2$ Nanosheets for High-Performance Photodetectors. *ACS Applied Nano Materials* **1**, 5414-5418 (2018).
22 Hong, Q. *et al.* Self-Powered Ultrafast Broadband Photodetector Based on p−n Heterojunctions of CuO/Si Nanowire Array. *ACS Applied Materials & Interfaces* **6**, 20887-20894 (2014).
23 Wu, F. *et al.* AsP/InSe Van der Waals Tunneling Heterojunctions with Ultrahigh Reverse Rectification Ratio and High Photosensitivity. *Advanced Functional Materials* **29** (2019).
24 Tong, T. *et al.* Sensitive and Ultrabroadband Phototransistor Based on Two-Dimensional Bi_2O_2Se Nanosheets. *Advanced Functional Materials* **29** (2019).
25 Atalla, M. R. M. & Koester, S. J. in *2017 75th Annual Device Research Conference (DRC)* (IEEE, South Bend, IN, USA, 2017).
26 Buscema, M. *et al.* Fast and Broadband Photoresponse of Few-Layer Black Phosphorus Field-Effect Transistors. *Nano Letters* **14**, 3347-3352 (2014).
27 Huang, L. *et al.* Waveguide-Integrated Black Phosphorus Photodetector for Mid-Infrared Applications. *ACS Nano* **13**, 913-921 (2019).
28 Wang, J. *et al.* Spectral Responsivity and Photoconductive Gain in Thin Film Black Phosphorus Photodetectors. *ACS Photonics* **6**, 3092-3099 (2019).
29 Huang, M. *et al.* Broadband Black-Phosphorus Photodetectors with High Responsivity. *Advanced Materials* **28**, 3481-3485 (2016).
30 Jia, J. *et al.* Avalanche Carrier Multiplication in Multilayer Black Phosphorus and Avalanche Photodetector. *Small* **15** (2019).
31 Tan, W. C. *et al.* A Black Phosphorus Carbide Infrared Phototransistor. *Advanced Materials* **30** (2018).
32 Feng, W., Zheng, W. & Hu, P. Solid-state reaction synthesis of two-dimensional $CuGaSe_2$ nanosheets for high performance photodetectors. *Physical Chemistry Chemical Physics* **16**, 19340-19344 (2014).
33 Hu, P. *et al.* Highly Responsive Ultrathin GaS Nanosheet Photodetectors on Rigid and Flexible Substrates. *Nano Letters* **13**, 1649-1654 (2013).
34 Hu, P., Wen, Z., Wang, L., Tan, P. & Xiao, K. Synthesis of Few-Layer GaSe Nanosheets for High Performance Photodetectors. *ACS Nano* **6**, 5988-5994 (2012).
35 Liu, F. *et al.* High-Sensitivity Photodetectors Based on Multilayer GaTe Flakes. *ACS Nano* **8**, 752-760 (2014).
36 Wei, J. *et al.* Zero-bias mid-infrared graphene photodetectors with bulk photoresponse and calibration-free polarization detection. *Nature Communications* **11**, 1-9 (2020).
37 Jacobs-Gedrim, R. B. *et al.* Extraordinary Photoresponse in Two-Dimensional In_2Se_3 Nanosheets. *ACS Nano* **8**, 514-521 (2014).
38 Island, J. O., Blanter, S. I., Buscema, M., Zant, H. S. J. v. d. & Castellanos-Gomez, A. Gate Controlled Photocurrent Generation Mechanisms in High-Gain In_2Se_3 Phototransistors. *Nano Letters* **15**, 7853-7858 (2015).

39 Lei, S. *et al.* An Atomically Layered InSe Avalanche Photodetector. *Nano Letters* **15**, 3048-3055 (2015).

40 Dai, M. *et al.* A Dual-Band Multilayer InSe Self-Powered Photodetector with High Performance Induced by Surface Plasmon Resonance and Asymmetric Schottky Junction. *ACS Nano* **12**, 8739-8747 (2018).

41 Jang, H. *et al.* High-Performance Near-Infrared Photodetectors Based on Surface-Doped InSe. *Advanced Functional Materials* **31** (2021).

42 Gao, A. *et al.* Observation of ballistic avalanche phenomena in nanoscale vertical InSe/BP heterostructures. *Nature Nanotechnology* **14**, 217-222 (2019).

43 Lv, L. *et al.* Reconfigurable two-dimensional optoelectronic devices enabled by local ferroelectric polarization. *Nature Communications* **10**, 1-10 (2019).

44 Wang, X. *et al.* Multimechanism Synergistic Photodetectors with Ultrabroad Spectrum Response from 375 nm to 10 μm. *Advanced Science* **6** (2019).

45 Dhyani, V. & Das, S. High-Speed Scalable Silicon-MoS_2 P-N Heterojunction Photodetectors. *Scientific Reports* **7**, 1-9 (2017).

46 Bullock, J. *et al.* Polarization-resolved black phosphorus/molybdenum disulfide mid-wave infrared photodiodes with high detectivity at room temperature. *Nature Photonics* **12**, 601-607 (2018).

47 Abderrahmane, A. *et al.* High photosensitivity few-layered $MoSe_2$ back-gated field-effect phototransistors. *Nanotechnology* **25** (2014).

48 Wu, G. *et al.* $MoTe_2$ p–n Homojunctions Defined by Ferroelectric Polarization. *Advanced Materials* **32** (2020).

49 Flöry, N. *et al.* Waveguide-integrated van der Waals heterostructure photodetector at telecom wavelengths with high speed and high responsivity. *Nature Nanotechnology* **15**, 118-124 (2020).

50 Maiti, R. *et al.* Strain-engineered high-responsivity $MoTe_2$ photodetector for silicon photonic integrated circuits. *Nature Photonics* **14**, 578-584 (2020).

51 Lu, Z. *et al.* Ultrahigh Speed and Broadband Few-Layer $MoTe_2$/Si 2D–3D Heterojunction-Based Photodiodes Fabricated by Pulsed Laser Deposition. *Advanced Functional Materials* **30** (2020).

52 Li, A. *et al.* Ultrahigh-Sensitive Broadband Photodetectors Based on Dielectric Shielded $MoTe_2$/Graphene/SnS_2 p–g–n Junctions. *Advanced Materials* **31**, 1805656 (2019).

53 Wang, Q. *et al.* van der Waals Epitaxial Ultrathin Two-Dimensional Nonlayered Semiconductor for Highly Efficient Flexible Optoelectronic Devices. *Nano Letters* **15**, 1183-1189 (2015).

54 Zeng, L.-H. *et al.* Controlled Synthesis of 2D Palladium Diselenide for Sensitive Photodetector Applications. *Advanced Functional Materials* **29** (2018).

55 Liu, E. *et al.* High Responsivity Phototransistors Based on Few-Layer ReS_2 for Weak Signal Detection. *Advanced Functional Materials* **26**, 1938-1944 (2016).

56 Zhou, X., Zhang, Q., Gan, L., Li, H. & Zhai, T. Large-Size Growth of Ultrathin SnS_2 Nanosheets and High Performance for Phototransistors. *Advanced Functional Materials* **26**, 4405-4413 (2016).

57 Zhou, X. *et al.* Ultrathin $SnSe_2$ Flakes Grown by Chemical Vapor Deposition for High-Performance Photodetectors. *Advanced Materials* **27**, 8035-8041 (2015).

58 Li, S., Zhang, Y., Yang, W., Liu, H. & Fang, X. 2D Perovskite $Sr_2Nb_3O_{10}$ for High-Performance UV Photodetectors. *Advanced Materials* **32** (2020).

59 Amani, M. *et al.* Solution-Synthesized High-Mobility Tellurium Nanoflakes for Short-Wave Infrared Photodetectors. *ACS Nano* **12**, 7253-7263 (2018).
60 Perea-López, N. *et al.* Photosensor Device Based on Few-Layered WS_2 Films. *Advanced Functional Materials* **23**, 5511-5517 (2013).
61 Tan, H. *et al.* Ultrathin 2D Photodetectors Utilizing Chemical Vapor Deposition Grown WS_2 With Graphene Electrodes. *ACS Nano* **10**, 7866-7873 (2016).
62 Lukman, S. *et al.* High oscillator strength interlayer excitons in two-dimensional heterostructures for mid-infrared photodetection. *Nature Nanotechnology* **15**, 675-682 (2020).
63 Mitta, S. B. *et al.* Gate-Modulated Ultrasensitive Visible and Near-Infrared Photodetection of Oxygen Plasma-Treated WSe_2 Lateral pn-Homojunctions. *ACS Applied Materials & Interfaces* **12**, 23261-23271 (2020).
64 Sun, J. *et al.* Lateral 2D WSe_2 p–n Homojunction Formed by Efficient Charge-Carrier-Type Modulation for High-Performance Optoelectronics. *Advanced Materials* **32** (2020).
65 Song, J. *et al.* High-efficiency and high-speed germanium photodetector enabled by multiresonant photonic crystal. *Nanophotonics* **10**, 1081-1087 (2020).
66 Tang, L. *et al.* Nanometre-scale germanium photodetector enhanced by a near-infrared dipole antenna. *Nature Photonics* **2**, 226-229 (2008).
67 Assefa, S., Xia, F. & Vlasov, Y. A. Reinventing germanium avalanche photodetector for nanophotonic on-chip optical interconnects. *Nature* **464**, 80-84 (2010).
68 Hu, X. *et al.* Halide-Induced Self-Limited Growth of Ultrathin Nonlayered Ge Flakes for High-Performance Phototransistors. *Journal of the American Chemical Society* **140**, 12909-12914 (2018).
69 Sistani, M., Böckle, R., Bartmann, M. G., Lugstein, A. & Weber, W. M. Bias-Switchable Photoconductance in a Nanoscale Ge Photodetector Operated in the Negative Differential Resistance Regime. *ACS Nano* **8**, 3469-3475 (2021).
70 Staudinger, P., Sistani, M., Greil, J., Bertagnolli, E. & Lugstein, A. Ultrascaled Germanium Nanowires for Highly Sensitive Photodetection at the Quantum Ballistic Limit. *Nano Letters* **18**, 5030-5035 (2018).
71 Xia, Z. *et al.* Single-crystalline germanium nanomembranephotodetectors on foreign nanocavities. *Science Advances* **3** (2017).
72 Yang, Y. *et al.* Ferroelectric Enhanced Performance of a GeSn/Ge Dual-Nanowire Photodetector. *Nano Letters* **20**, 3872-3879 (2020).
73 Yu, X. *et al.* Narrow bandgap oxide nanoparticles coupled with graphene for high performance mid-infrared photodetection. *Nature Communications* **9**, 1-8 (2018).
74 Li, X. *et al.* High detectivity graphene-silicon heterojunction photodetector. *Small* **12**, 595-601 (2016).
75 Liu, C.-H., Chang, Y.-C., Norris, T. B. & Zhong, Z. Graphene photodetectors with ultra-broadband and high responsivity at room temperature. *Nature Nanotechnology* **9**, 273-278 (2014).
76 Wei, W. *et al.* Direct Heteroepitaxy of Vertical InAs Nanowires on Si Substrates for Broad Band Photovoltaics and Photodetection. *Nano Letters* **9**, 2926-2934 (2009).
77 Mauthe, S. *et al.* High-speed III-V nanowire photodetector monolithically integrated on Si. *Nature Communications* **11**, 1-7 (2020).

78 Um, D.-S. *et al.* InGaAs Nanomembrane/Si van der Waals Heterojunction Photodiodes with Broadband and High Photoresponsivity. *ACS Applied Materials & Interfaces* **8**, 26105-26111 (2016).
79 Guo, N. *et al.* Light-Driven WSe_2-ZnO Junction Field-Effect Transistors for High-Performance Photodetection. *Advanced Science* **7** (2020).
80 Retamal, J. R. D. *et al.* Concurrent Improvement in Photogain and Speed of a Metal Oxide Nanowire Photodetector through Enhancing Surface Band Bending via Incorporating a Nanoscale Heterojunction. *ACS Photonics* **1**, 354-359 (2014).
81 Zhou, W. *et al.* Solution-processed Upconversion Photodetectors Based on Quantum dots. *Nature Electronics* **3**, 251-258 (2020).
82 Prins, F. *et al.* Fast and Efficient Photodetection in Nanoscale Quantum-Dot Junctions. *Nano Letters* **12**, 5740-5743 (2012).
83 Feng, J. *et al.* Single-crystalline layered metal-halide perovskite nanowires for ultrasensitive photodetectors. *Nature Electronics* **1**, 404-410 (2018).
84 Cao, F. *et al.* Novel perovskite/TiO_2/Si trilayer heterojunctions for high-performance self-powered ultraviolet-visible-near infrared (UV-Vis-NIR) photodetectors. *Nano Research* **11**, 1722-1730 (2018).
85 Yang, W. *et al.* High-Performance Silicon-Compatible Large-Area UV-to-Visible Broadband Photodetector Based on Integrated Lattice-Matched Type II Se/n-Si Heterojunctions. *Nano Letters* **18**, 4697-4703 (2018).
86 Du, W., Inokawa, H., Satoh, H. & Ono, A. SOI metal-oxide-semiconductor field-effect transistor photon detector based on single-hole counting. *Optics Letters* **36**, 2800-2802 (2011).
87 Fan, P. *et al.* An invisible metal-semiconductor photodetector. *Nature Photonics* **6**, 380-385 (2012).
88 Zhou, X. *et al.* High performance near-infrared photodetectors based on ultrathin SnS nanobelts grown via physical vapor deposition. *Journal of Materials Chemistry C* **4**, 2111-2116 (2016).
89 Yang, J. *et al.* Ultra-Broadband Flexible Photodetector Based on Topological Crystalline Insulator SnTe with High Responsivity. *Small* **14** (2018).
90 Ji, T. *et al.* An Interface Engineered Multicolor Photodetector Based on n-Si(111)/TiO_2 Nanorod Array Heterojunction. *Advanced Functional Materials* **26**, 1400-1410 (2016).
91 Wang, L. *et al.* MoS_2/Si Heterojunction with Vertically Standing Layered Structure for Ultrafast, High-Detectivity, Self-Driven Visible–Near Infrared Photodetectors. *Advanced Functional Materials* **25**, 2910-2919 (2015).
92 Mao, J. *et al.* Ultrafast, Broadband Photodetector Based on $MoSe_2$/Silicon Heterojunction with Vertically Standing Layered Structure Using Graphene as Transparent Electrode. *Advanced Science* **3** (2016).
93 Wang, Z. *et al.* Optimizing Performance of Silicon-Based p–n Junction Photodetectors by the Piezo-Phototronic Effect. *ACS Nano* **8**, 12866-12873 (2014).
94 Yao, J., Deng, Z., Zheng, Z. & Yang, G. Stable, Fast UV−Vis−NIR Photodetector with Excellent Responsivity, Detectivity, and Sensitivity Based on α-In_2Te_3 Films with a Direct Bandgap. *ACS Applied Materials & Interfaces* **8**, 20872-20879 (2016).
95 Chen, S. *et al.* Facile Synthesis of γ-In_2Se_3 Nanoflowers toward High Performance Self-Powered Broadband γ-In_2Se_3/Si Heterojunction Photodiode. *Small* **13** (2017).